Journal of VLSI Signal Processing 23, 351–371 (1999)


# On the Design of Second Order Dynamics Reaction-Diffusion CNNs

T. SERRANO-GOTARREDONA AND A. RODRÍGUEZ-VÁZQUEZ
*Instituto de Microelectrónica de Sevilla, Centro Nacional de Microelectrónica, Ed. Cica, Avda. Reina Mercedes s/n. Sevilla 41012, Spain*

**Abstract.** In this paper, a second order reaction-diffusion equation has been identified which is able to reproduce through parameter setting a rich variety of spatio-temporal behaviors. It has been shown that these behaviors are robust against wide random variations in the equation parameters. We have designed a hardware that implements the log-domain version of the selected reaction-diffusion equation. The logarithmic compression of the state variables allows several decades of variation of these state variables without saturation. Furthermore, as all the equation parameters are implemented as currents, they can be adjusted several decades. The correct operation of the hardware has been verified through HSPICE simulations.

## I. Introduction

Many pattern formation and wave propagation phenomena that appear in nature can be described as *local* interactions among cells located at the knots of a regular array; each cell in the array exhibiting *complex nonlinear dynamics*, i.e. nonlinear dynamics of order larger than one. Such a network can be considered a CNN of complex dynamic cells [1].

These wave formation phenomena are exhibited by systems belonging to very different scientific disciplines. For example, in neurophysiology, the propagation of electrical impulses through the nervous system, or the propagation of the cardiac movement through the cardiac muscle are classical examples of active wave propagation.

Active wave propagation differs in some sense from the propagation of classical waves. Table 1 highlights some of the differences between the behavior of classical waves and active ones [2]. The most relevant autowaves propagation characteristic is the non conservation of energy. This is due to the fact that *active* waves propagate in an active medium, that is, a medium that provides energy to the propagating perturbation. As a consequence, the perturbation propagates in the medium without decaying; the medium restores the amplitude of the perturbation during the propagation process.

One of the most interesting active mediums known is the human body. Regarding the human body as an active medium, it is known that anomalies causing disorganization of autowave structures result into patient's clinical syndromes [3–6]. Thus, a new scientific trend in medicine is emerging that studies the processes of formation, support and disintegration of autowave structures in the active media of the human body. Many research groups are investigating these phenomena through *computer simulation* [5–7]. However, the huge amount of calculations involved in the simulations of these spatio-temporal phenomena makes the process tedious and extremely time consuming. In such an scenario, the existence of a specialized *parallel-processing hardware* able to reproduce these behaviors at very high speed, would be a valuable tool to study and understand more deeply these phenomena.

In this paper, we present an *analog array processor chip* which is capable to robustly reproduce the rich phenomenology associated with active wave propagation and pattern formation. In Section II, we will see how these phenomena can be mathematically described by non-linear differential equations. These equations can be spatially discretized and mapped onto a CNN array of complex dynamics cells. In Section III, we select an equation which is the simplest one that preserve the capability of generating patterns and reproduce a wide variety of wave propagation phenomena.

*Table 1.* Properties of active wave and classical wave propagation.

| Properties | Classical waves | Active waves |
|---|---|---|
| Conservation of energy | + | − |
| Conservation of amplitude | − | + |
| Reflection | + | − |
| Annihilation | − | + |
| Interference | + | − |
| Diffraction | + | + |

We show simulation results of different spatio-temporal behaviors. Also, it is shown that the same behaviors are reproduced with random variations in the equation parameters wider than 20%. In Section IV, we introduce the log-domain synthesis method. A log-domain circuit that implements the selected reaction-diffusion equation is presented in Section V. HSPICE simulations that validate the correct operation of the designed hardware are shown in Section VI. Finally, in Section VII, we draw some conclusions.

## II. Reaction-Diffusion CNN

The behaviors underlying the generation of patterns and active wave phenomena can be described by systems of nonlinear differential equations, generally known as *reaction-diffusion* equations [8]. They have the general form,

$$\frac{\partial}{\partial t}\boldsymbol{u} = \boldsymbol{f}(\boldsymbol{u}) + D\nabla^2\boldsymbol{u}, \tag{1}$$

where $\boldsymbol{u}(\boldsymbol{x}, t)$ is an m-dimensional vector which defines the system state at position $\boldsymbol{x}$ (where $\boldsymbol{x} \in \mathcal{R}^n$) at time $t$. $\boldsymbol{f}(\boldsymbol{u})$ is a set of $m$ nonlinear functions of the state variable vector $\boldsymbol{u}$. $D$ is an $m \times m$ matrix. The diagonal elements of $D$, $D_i$ are known as the diffusion coefficients of the $i$-th state variable. And $\nabla^2$ is the Laplacian operator, which defined in $\mathcal{R}^2$ is,

$$\nabla^2 u_l = \frac{\partial^2 u_l}{\partial x^2} + \frac{\partial^2 u_l}{\partial y^2} \quad l = 1, 2, \ldots, m. \tag{2}$$

Table 2 contains some well-known reaction-diffusion equations commonly used in the literature [9–14]

*Table 2.* Reaction-diffusion equations reported in literature to describe active systems pertaining to several scientific disciplines.

| Discipline | Equation | |
|---|---|---|
| Genetic | Fisher's Equation | $\frac{\partial u}{\partial t} = u(1-u) + \nabla^2 u$ |
| Biology | Meinhardt-Gierer | $\frac{\partial u}{\partial t} = \alpha\frac{u^2}{v} - \beta v + D_1\nabla^2 u$ |
| | | $\frac{\partial v}{\partial t} = \alpha u^2 - \gamma v + D_2\nabla^2 v$ |
| Thermodynamics | Brusselator | $\frac{\partial u}{\partial t} = a - (b+1)u + u^2 v + D_1\nabla^2 u$ |
| | | $\frac{\partial v}{\partial t} = bu - u^2 v + D_2\nabla^2 v$ |
| Neurophysiology | FitzHugh-Nagumo | $\frac{\partial u}{\partial t} = -\left(\frac{u^3}{3} - u\right) + D_1\nabla^2 u$ |
| | | $\frac{\partial v}{\partial t} = \varepsilon(u - bv)$ |
| | Hodgin-Huxley | $\frac{\partial u}{\partial t} = -f(u) + D_1\nabla^2 u$ |
| | | $\frac{\partial v}{\partial t} = g_v(u)(1-v) - h_v(u)\,v$ |
| | | $\frac{\partial m}{\partial t} = g_m(u)(1-m) - h_m(u)m$ |
| | | $\frac{\partial n}{\partial t} = g_n(u)(1-n) - h_n(u)n$ |
| Chemistry | Oregonator | $\varepsilon\frac{\partial u}{\partial t} = u + v - \alpha u^2 + D_1\nabla^2 u$ |
| | | $\frac{\partial v}{\partial t} = -v + \beta m - uv + D_2\nabla^2 v$ |
| | | $\delta\frac{\partial}{\partial t} m = u - m + D_3\nabla^2 m$ |

to model complex spatio-temporal behaviors that appear in several disciplines. All the equations in Table 2 correspond to the general form of (1). These equations can generate patterns and waves including *travelling* waves, *trigger* waves and *spiral* waves.

These phenomena have been also successfully reproduced in case the continuum medium description is approximated by a *discretely spaced* one [15–17]. If we do this spatial discretization, Eq. (1) takes the form,

$$\frac{d}{dt}\boldsymbol{u}(i,j) = f(\boldsymbol{u}(i,j)) + D[\boldsymbol{u}(i+1,j) + \boldsymbol{u}(i,j+1) + \boldsymbol{u}(i-1,j) + \boldsymbol{u}(i,j-1) - 4\boldsymbol{u}(i,j)], \quad (3)$$

where $\boldsymbol{u}(i, j)$ is the vector of state variables for the cell located at spatial position $(i, j)$.

Equation (3) can be interpreted as a regular array of cells (CNN). Each cell has complex dynamics described by $m$ state variables and is coupled to its neighbors through linear *synapses* [1].

## III. Selection of an Equation

Equations in Table 2, show different levels of complexity, that is, number of state variables, number and type of nonlinearities and number of couplings between state variables of adjacent cells. Our design objective is to select an equation that captures all the spatio-temporal behaviors listed in Table 2 (i.e., Turing pattern formation, traveling waves, trigger waves and spiral waves propagation), while at the same time maintains the lowest possible level of complexity.

The selected equation that fulfills the above requirements is,

$$\begin{aligned} \frac{du}{dt} &= -f(u) - gv + D_u\nabla^2 u \\ \frac{dv}{dt} &= \varepsilon(u + \beta - \gamma v + D_v\nabla^2 v) \end{aligned}, \quad (4)$$

where the nonlinear term $f(u)$ has been approximated by the *piecewise-linear* nonlinearity depicted in Fig. 1.

Through proper parameter setting, this equation is able to exhibit Turing's patterns formation, trigger wave, travelling wave propagation and spiral wave formation. On the other hand, the equation exhibit some features which render it very well suited for circuit realization:

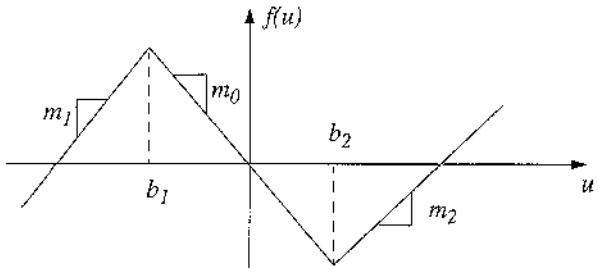


$$f(u) = \begin{cases} m_1 u + b_1(m_0 - m_1) & u \le b_1 \\ m_0 u & b_1 \le u \le b_2 \\ m_2 u + b_2(m_0 - m_2) & b_2 \le u \end{cases}$$

*Figure 1.* Piecewise-linear approximation of the nonlinearity of Eq. (4).

1. There is only one nonlinear term which has been approximated by a piecewise-linear nonlinearity. These nonlinearities are simpler to implement than any other type [18].
2. There are only two state variables per cell. It has been shown elsewhere [16], that a second order behavior with a slow-fast regime is required to achieve spiral wave formation.
3. There are only two coupling terms between the two state variables of adjacent cells. A double coupling between the two state variables of neighbor cells with very different coupling strengths ($D_u \ll D_v$) is needed to reproduce Turing's pattern formation [17].

Table 3 shows sets of parameter values to generate traveling wave, trigger wave propagation, spiral wave formation and formation of blobs Turing patterns, and stripped Turing patterns, using Eq. (4).

### *III.A. One Dimensional Case*

A one dimensional array of $N = 32$ cells has been simulated in MATLAB. The cell parameters were set to obtain two different behaviors: a travelling wave propagating with constant amplitude through the array and a trigger wave behavior.

Figure 2 shows the propagation of a traveling wave. For this simulation the parameters of the cells were set to $m_1 = m_2 = 1$, $m_0 = -1$, $b_1 = -1$, $b_2 = 1$, $\varepsilon = 1/35$, $\beta = 0.7$, $\gamma = 1.2$ and $g = 1$. The coupling parameters were set to $D_u = 0.3$ and $D_v = 0$. Figure 2(a) shows different snapshots that represent the $u$ state variable as a function of the position of the cell in the

*Table 3.* Parameter settings of Eq. (4) that generate different spatio-temporal behaviours.

| | $m_0$ | $m_1$ | $m_2$ | $b_1$ | $b_2$ | $\varepsilon$ | $\beta$ | $\gamma$ | $g$ | $D_u$ | $D_v$ |
|---|---|---|---|---|---|---|---|---|---|---|---|
| Travelling wave | −1 | 1 | 1 | −1 | 1 | 1/35 | 0.7 | 1.2 | 1 | 0.3 | 0 |
| Trigger wave | −0.8 | 1 | 1 | −1 | 1 | 1/35 | 0.7 | 3 | 1 | 0.2 | 0 |
| Spiral wave | −0.5 | 1 | 1 | −1 | 5 | 1/35 | 0.7 | 1.2 | 1 | 0.1 | 0 |
| Turing's patterns (blobs) | −0.1 | 1 | 1 | −1 | 10 | 1/35 | 0 | 6 | 1 | 0.1 | 50 |
| Turing's patterns (stripes) | −0.1 | 1 | 1 | −1 | 1 | 1/10 | 0 | 2 | 1 | 0.1 | 50 |

array. The snapshots are taken every 10 s. Figure 2(b) depicts the same representation but for the second state variable $v$.

The propagation of a trigger wave is illustrated in Fig. 3. Initially all the cells are in the equilibrium state $P_1$, with $u_1 = 1.18$ and $v_1 = 0.63$. The $u$ state variable of the first cell in the array is perturbed to a non resting state with $u_p = -1.52$. This cell evolves towards a new equilibrium $P_2$ characterized by $u_2 = -1.52$ and $v_2 = -0.28$. The perturbation propagates through the array, triggering all the cells in the array to the $P_2$ state. For the simulation in Fig. 3, the parameters of the cells were set to $m_1 = m_2 = 1$, $m_0 = -0.8$, $b_1 = -1$, $b_2 = 1$, $\varepsilon = 1/35$, $\beta = 0.7$, $\gamma = 3$, $g = 1$, and the coupling parameters were $D_u = 0.2$ and $D_v = 0$. Figure 3(a) shows the snapshots of the $u$ state variable observed every 20 s. Figure 3(b) shows the same plots for the $v$ state variable.

We have found that there are points in the parameter space where the traveling wave behavior is robust against cell parameter random deviations as wide as 20%. For example, for nominal cell parameters $m_1 = m_2 = 1$, $m_0 = -0.9$, $b_1 = -1$, $b_2 = 1$, $\varepsilon = 1/35$, $\beta = 0.55$, $\gamma = 1.2$, $g = 1$, and coupling parameters $D_u = 0.5$ and $D_v = 0$, the traveling wave behavior is robust against random deviations with a standard deviation up to a 20%. Deviations were introduced not only in the cell parameters, but also in the coupling parameter $D_u$.

The robustness of the behavior has been checked also for the trigger wave propagation. A tolerance of a standard deviation of 20% in the cell parameters and coupling parameters has been found through MATLAB simulations. In these simulations, the cell parameters were set to $m_1 = m_2 = 1$, $m_0 = -0.8$, $b_1 = -1$, $b_2 = 1$, $\varepsilon = 1/35$, $\beta = 0.7$, $\gamma = 5$, $g = 1.2$, and the coupling parameters were $D_u = 0.5$ and $D_v = 0$.

### *III.B. Two Dimensional Case*

MATLAB simulations have been performed on a two dimensional array of $N \times N = 32 \times 32$ cells. In this

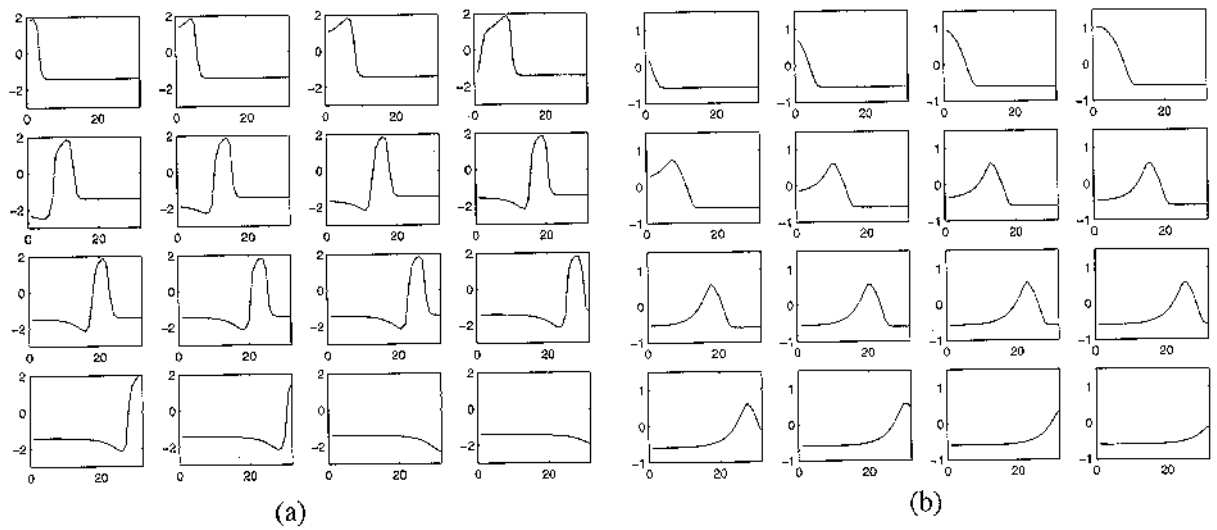


*Figure 2.* Simulation of a travelling wave propagating through a one dimensional array of $N = 32$ cells. (a) $u$ state variable, and (b) $v$ state variable.

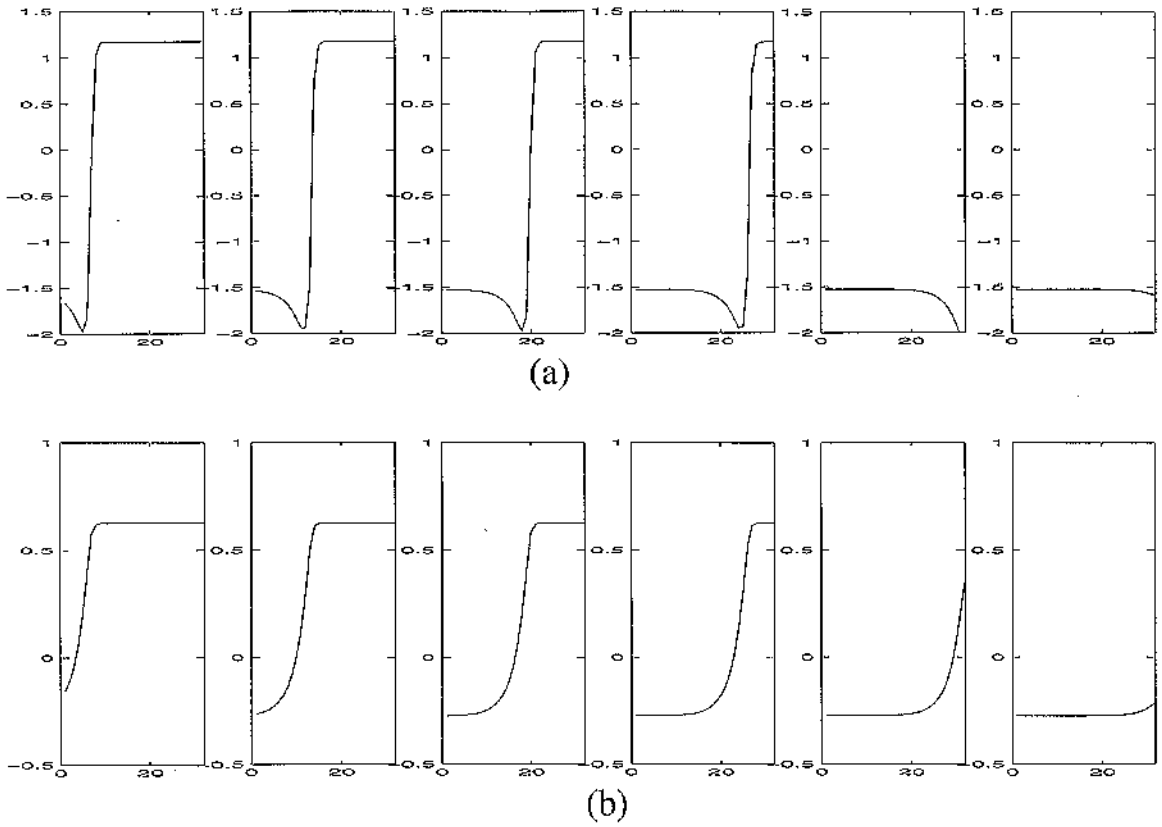


*Figure 3.* Simulation of a trigger wave propagating through a one dimensional array of $N = 32$ cells. (a) $u$ state variable, and (b) $v$ state variable.

case, simulations have been focused on confirming the phenomena of spiral waves and Turing's patterns formation.

The spiral wave formation phenomena is illustrated in the simulation of Fig. 4. The cell parameters for this simulation are set to $m_1 = m_2 = 1$, $m_0 = -0.5$, $b_1 = -1$, $b_2 = 5$, $\varepsilon = 1/35$, $\beta = 0.7$, $\gamma = 1.2$ and $g = 1$. The coupling parameters are $D_u = 0.1$ and $D_v = 0$. Appropriate initial conditions are given to the cells. The initial perturbation creates a spiral wave that maintains the medium permanently oscillating. Figure 4(a) shows snapshots of the $u$ state variable observed every 12.5 s, while Fig. 4(b) shows the same snapshots for the $v$ state variable.

The formation of Turing's patterns has also been verified. Figure 5 depicts the Turing's patterns generated for cell parameters set to $m_1 = m_2 = 1$, $m_0 = -0.1$, $b_1 = -1$, $b_2 = 10$, $\varepsilon = 1/35$, $\beta = 0.0$, $\gamma = 6$ and $g = 1$. The coupling parameters were set to $D_u = 0.1$ and $D_v = 50$. With this parameters a pattern of blobs is generated as shown in Fig. 5. Figure 5 shows the resulting pattern generated in the $u$ state variable with the image coded in a scale of gray levels.

Monte Carlo simulations of the different behaviors in a two dimensional array of $N \times N = 32 \times 32$ cells have also been performed. Robustness of all the behaviors to standard deviations higher than 20% has been found. Table 4 shows, for different spatio-temporal

*Table 4.* Tolerance in the parameter deviations of different spatio-temporal behaviors.

| | $m_0$ | $m_1$ | $m_2$ | $b_1$ | $b_2$ | $\varepsilon$ | $\beta$ | $\gamma$ | $g$ | $D_u$ | $D_v$ | $\sigma$ |
|---|---|---|---|---|---|---|---|---|---|---|---|---|
| Travelling wave | −0.9 | 1 | 1 | −1 | 1 | 1/35 | 0.55 | 1.2 | 1.1 | 0.5 | 0 | 25% |
| Trigger wave | −0.9 | 1 | 1 | −1 | 1 | 1/35 | 0.7 | 5 | 1.2 | 0.5 | 0 | 30% |
| Spiral wave | −0.5 | 1 | 1 | −1 | 5 | 1/35 | 0.7 | 1.2 | 1 | 0.1 | 0 | 20% |
| Turing's patterns | −0.1 | 1 | 1 | −1 | 10 | 1/35 | 0 | 6 | 1 | 0.1 | 50 | 30% |

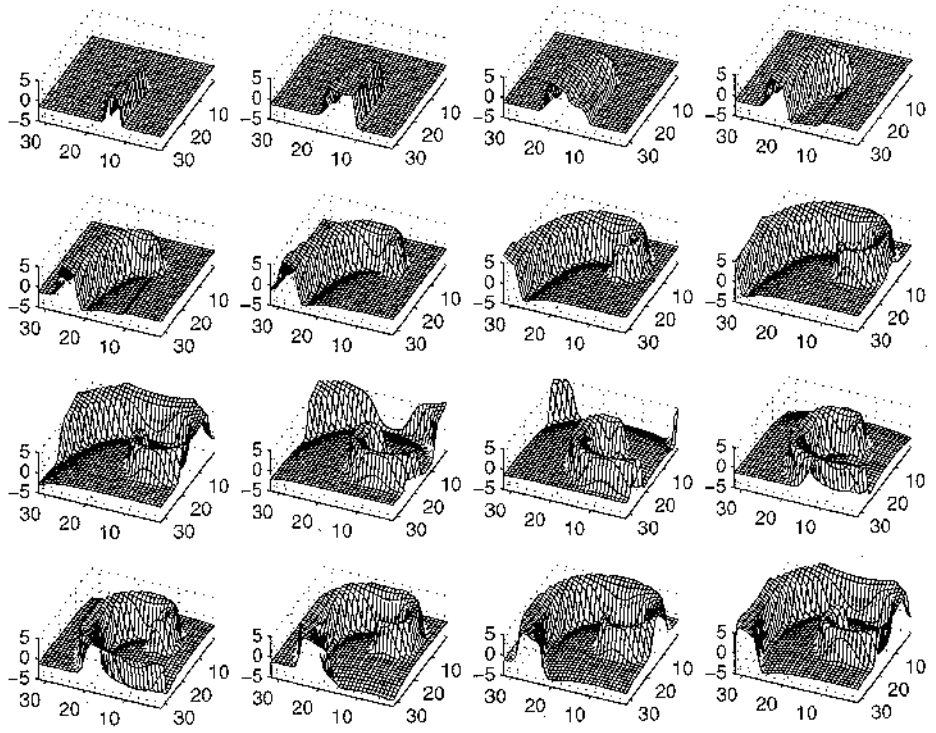


(a)

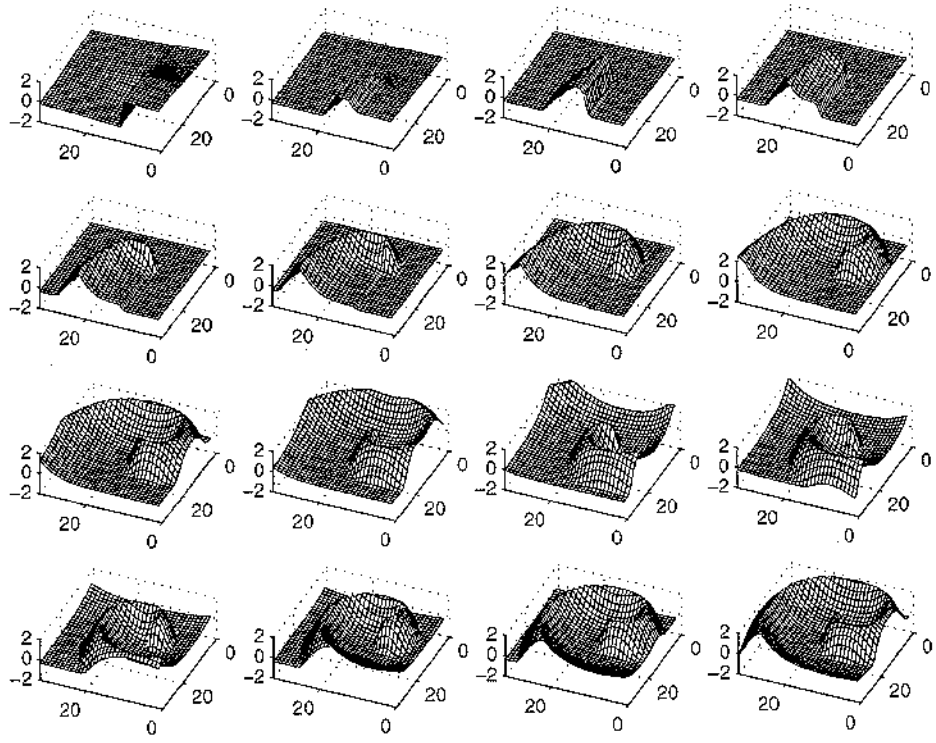


(b)

*Figure 4.* Spiral wave formation in an array of $N \times N = 32 \times 32$ cells. (a) $u$ state variable, and (b) $v$ state variable.

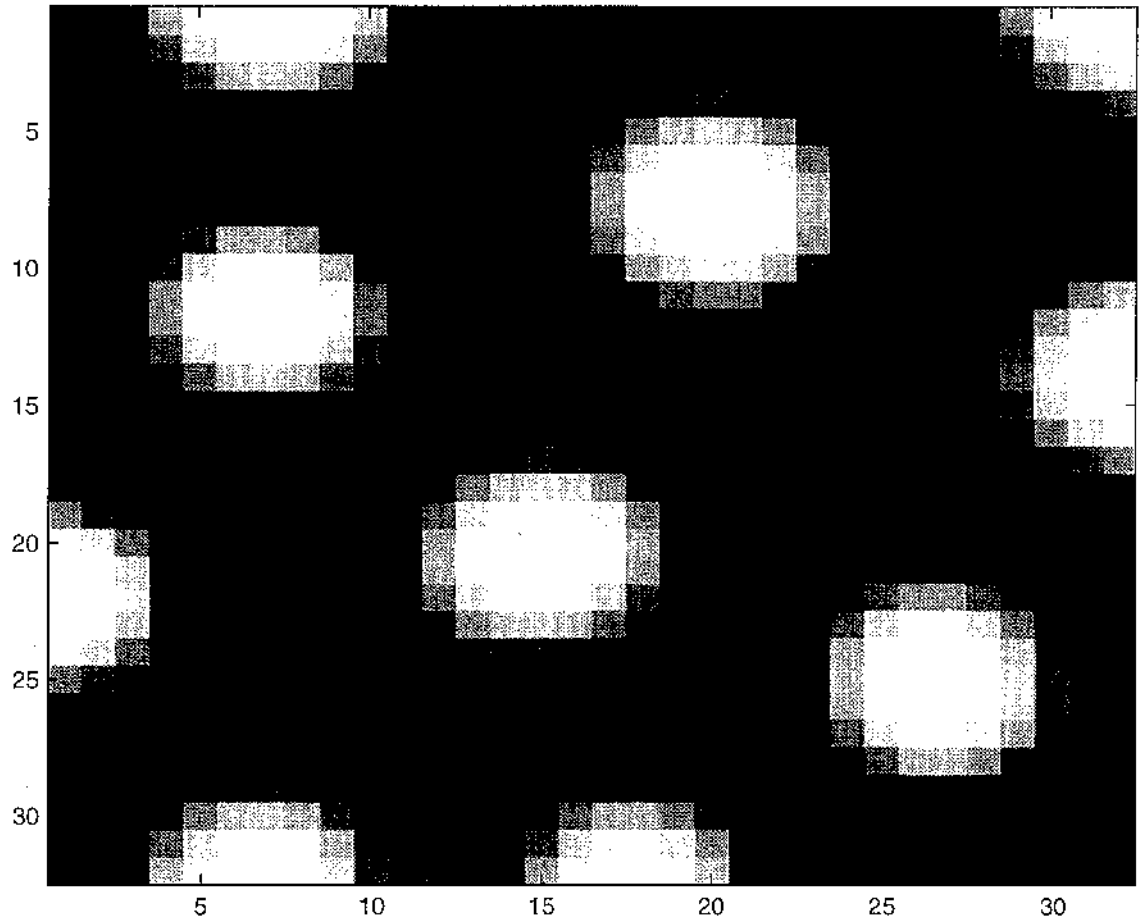


*Figure 5.* Formation of Turing's patterns. (a) Pattern developed for the $u$ state variable with the image coded as levels of gray.

behaviors, the maximum standard deviations allowed simultaneously in all the cell parameters and coupling parameters that maintain the same qualitative behavior in all the cells in the array. Also shown in Table 4 are the nominal cell and coupling parameters used in the different simulations.

The robustness of Turing's patterns formation against random parameter deviations is illustrated in Fig. 6. A Monte Carlo simulation with random deviations of $\sigma = 30\%$ was performed. The deviations were introduced not only in the cell parameters but also in the coupling parameters between cells. The nominal parameters in this simulation are the same used in the simulation of Fig. 5 and listed in Table 4, i.e., $m_1 = m_2 = 1, m_0 = -0.1, b_1 = -1, b_2 = 10, \varepsilon = 1/35, \beta = 0.0, \gamma = 6, g = 1$ and coupling parameters $D_u = 0.1$ and $D_v = 50$. Figure 6 shows the result of this simulation. Figure 6 shows the final pattern developed in the $u$ state variable with the values of the $u$ state variable coded as levels of gray.

## IV. Log-Domain Synthesis

Our target is to synthesize an array of $N \times N = 32 \times 32$ second order cells implementing the discretely spaced version of the nonlinear differential Eq. (4),

$$\begin{aligned}\tau \frac{d}{dt}u(i,j) &= -f(u(i,j)) - gv(i,j) \\ &\quad + D_u(u(i+1,j) + u(i,j+1) \\ &\quad + u(i-1,j) + u(i,j-1) - 4u(i,j)) \\ &\qquad i = 1, 2, \ldots, N \\ \frac{\tau d}{\varepsilon dt}v(i,j) &= u(i,j) + \beta - \gamma v(i,j) \\ &\quad + D_v(v(i+1,j) + v(i,j+1) \\ &\quad + v(i-1,j) + v(i,j-1) - 4v(i,j)) \\ &\qquad j = 1, 2, \ldots, N \end{aligned} \tag{5}$$

were the continuous two dimensional Laplacian

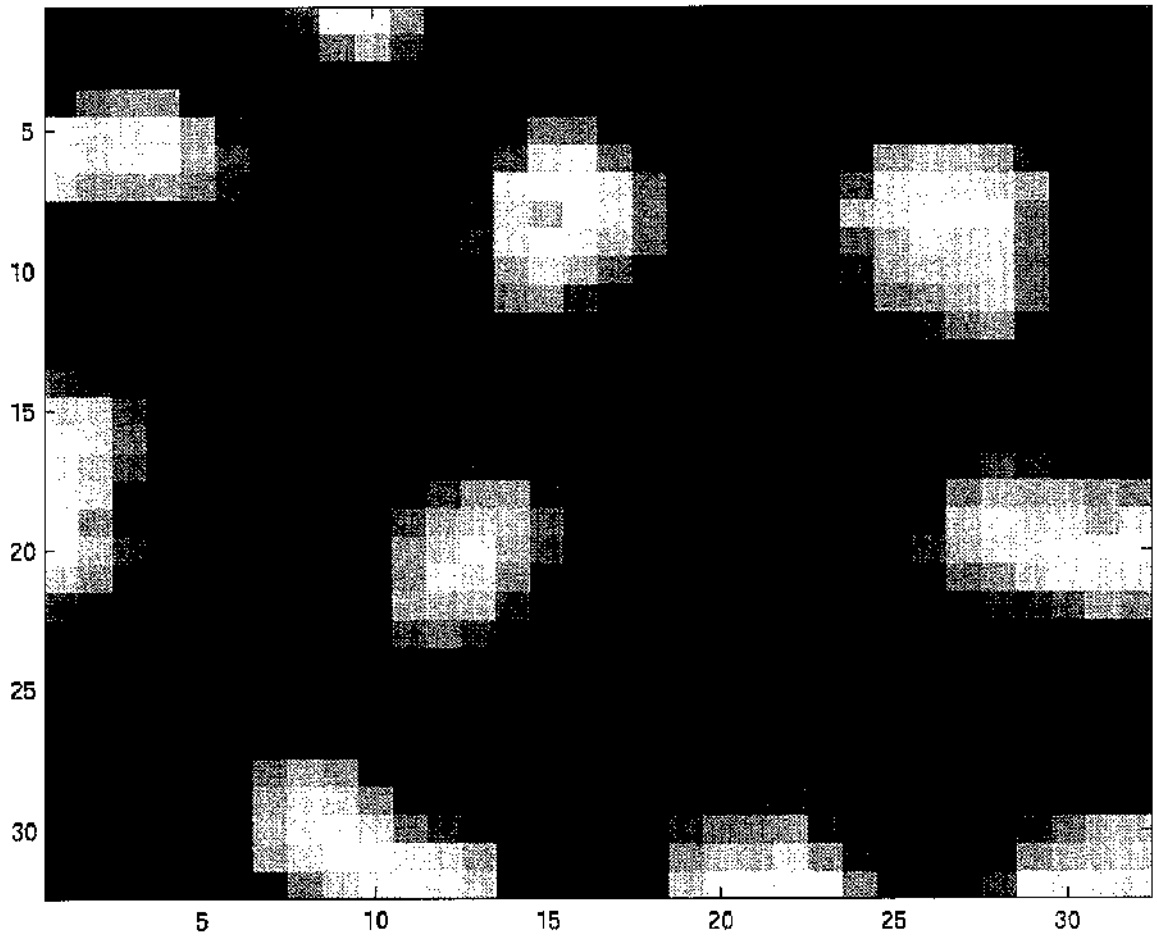


*Figure 6.* Monte Carlo Simulation of the formation of Turing's patterns in an array of $N \times N = 32 \times 32$ cells. Final pattern obtained in the $u$ state variable with the $u$ values coded in a scale of gray levels.

operator has been substituted by its discretized version (see Eq. (3)).

In order to reproduce different spatio-temporal phenomena through parameter setting, the hardware must have the following properties:

1. Parameters must be tunable in a wide range without degrading the behaviors.
2. State variables $u$ and $v$ must have a wide range of operation without saturation of the behavior.
3. To guarantee observability of the output waves, the time constant must be scalable to arbitrarily low values.

These requirements are met in a log-domain implementation [19–22]. In a log-domain circuit the voltages in the circuit nodes are a logarithmically compressed version of the state variables. Thus, the state variables can vary several decades without saturation of the behavior. Also the cell parameters are currents that can be adjusted several decades in the MOS subthreshold regime [23, 24]. Furthermore, it is possible to scale down simultaneously all the currents in the circuit making the operation arbitrarily slow.

In the proposed circuit implementation we have to distinguish between mathematical state variables and circuital state variables. The mathematical state variables, $u(i, j)$ and $v(i, j)$ in Eq. (5), are currents. However, it does not mean that the dynamic elements of the circuit implementation are inductors. They are actually capacitors. The voltages associated to these capacitors define the circuital state variables, $v_u(i, j)$ and $v_v(i, j)$, which are related to the mathematical state variables by,

$$\begin{aligned} u &= I_s \exp(\alpha v_u) \\ v &= I_s \exp(\alpha v_v) \end{aligned} \quad . \tag{6}$$

The first thing to note is that this mapping is valid only if $u$ and $v$ are positive. If this is not the case a

coordinate transformation of the mathematical state vector can always be made that transforms a system with negative state variable values into a system with only positive ones [21]. Suppose a translation and a scaling of the state variable vector is made,

$$\begin{aligned} u_n &= \delta u + u_0 \\ v_n &= \delta v + v_0 \end{aligned}, \tag{7}$$

where $(u_0, v_0)$ is the translation vector and $\delta$ is the scaling factor.

After substituting the original state variables, $u$ and $v$, of Eq. (4) by the scaled and translated variables $u_n$ and $v_n$, the following differential equation results,

$$\begin{aligned} \tau \frac{du_n}{dt} &= -f(u_n) - g v_n + u_{\text{off}} + D_u \nabla^2 u_n \\ \frac{\tau}{\varepsilon}\frac{dv_n}{dt} &= u_n + \beta_n - \gamma v_n + v_{\text{off}} + D_v \nabla^2 v_n \end{aligned}, \tag{8}$$

where $\beta_n = \delta\beta$, and the breakpoints of the piecewise-linear nonlinearity have been redefined as:

$$\begin{aligned} b_{1_n} &= \delta b_1 + u_o \\ b_{2_n} &= \delta b_2 + u_o \end{aligned} \tag{9}$$

Terms $u_{\text{off}}$ and $v_{\text{off}}$ are two offset terms defined as:

$$\begin{aligned} u_{\text{off}} &= g v_0 + m_0 u_0 \\ v_{\text{off}} &= -u_0 + \gamma v_0 \end{aligned}. \tag{10}$$

Applying the log-domain mapping given by (6) to the discretely spaced version of Eq. (8) that results after the translation and scaling of the state variables, yields the following log-domain equation,

$$\begin{aligned} C_u \dot{v}_u &= -f(u) e^{-\alpha v_u} - I_g e^{\alpha(v_v - v_u)} + I_{uo} e^{-\alpha v_u} \\ &\quad + \text{Coupling}_u \\ C_v \dot{v}_v &= I_e e^{\alpha(v_u - v_v)} + I_\beta e^{-\alpha v_v} - I_\gamma + \text{Coupling}_v \end{aligned} \tag{11}$$

where the terms called *Coupling* account for the Laplacian operator and are given as:

$$\begin{aligned} \text{Coupling}_u &= I_{du}\left(e^{\alpha(v_u(i+1,j)-v_u)} + e^{\alpha(v_u(i,j+1)-v_u)}\right. \\ &\quad \left. + e^{\alpha(v_u(i-1,j)-v_u)} + e^{\alpha(v_u(i,j-1)-v_u)} - 4\right) \\ \text{Coupling}_v &= I_{dv}\left(e^{\alpha(v_v(i+1,j)-v_v)} + e^{\alpha(v_v(i,j+1)-v_v)}\right. \\ &\quad \left. + e^{\alpha(v_v(i-1,j)-v_v)} + e^{\alpha(v_v(i,j-1)-v_v)} - 4\right) \end{aligned} \tag{12}$$

Notice that the translated and scaled state variables have been renamed as $u$ and $v$ for shortness of notation and, $v_u$ and $v_v$ are the voltages that are logarithmically related with the translated and scaled state variables $u$ and $v$, as given by Eq. (6). Parameters in Eqs. (11) and (12) are related with the ones in Eq. (8) through the following relations,

$$\begin{aligned} C_u &= \alpha \tau I_s \\ \frac{C_v}{C_u} &= \frac{I_e}{\varepsilon I_s} \\ I_g &= g I_s \\ I_{uo} &= u_{\text{off}} \\ I_{du} &= D_u I_s \\ I_\beta &= (\beta_n + v_{\text{off}})\frac{I_e}{I_s} \\ I_\gamma &= \gamma I_e \\ I_{dv} &= D_v I_e \end{aligned}, \tag{13}$$

where, as it will become clear later, in our implementation $I_s$ is a free design current parameter that for a given capacitance $C_u$ controls the characteristic time constant of the response $\tau$. Reducing current $I_s$, the global response of the circuit can be appropriately slowed down. $I_e$ is also a current parameter that, for a given relation between capacitances $C_v/C_u$, must be tuned to set the original parameter $\varepsilon$ to its appropriate value.

## V. Circuit Implementation

Circuit implementation is focused on the realization of (11) and (12), and will be explained in two steps:

- implementation of the core cell dynamics (Eq. (11)), excluding coupling,
- implementation of the coupling terms (Eq. (12)).

### *V.A. The Uncoupled Cell*

Each uncoupled cell has a second order dynamics described by:

$$\begin{aligned} C_u \dot{v}_u &= -f(u) e^{-\alpha v_u} - I_g e^{\alpha(v_v - v_u)} + I_{uo} e^{-\alpha v_u} \\ C_v \dot{v}_v &= I_e e^{\alpha(v_u - v_v)} + I_\beta e^{-\alpha v_v} - I_\gamma \end{aligned}, \tag{14}$$

as derived from (11) by making the coupling terms null.

Figure 7 shows the block diagram of the circuit implementing Eq. (14). The blocks denoted as $E+$ and $E-$ are transconductors obeying an exponential law [20, 21]. That is, the output current of these

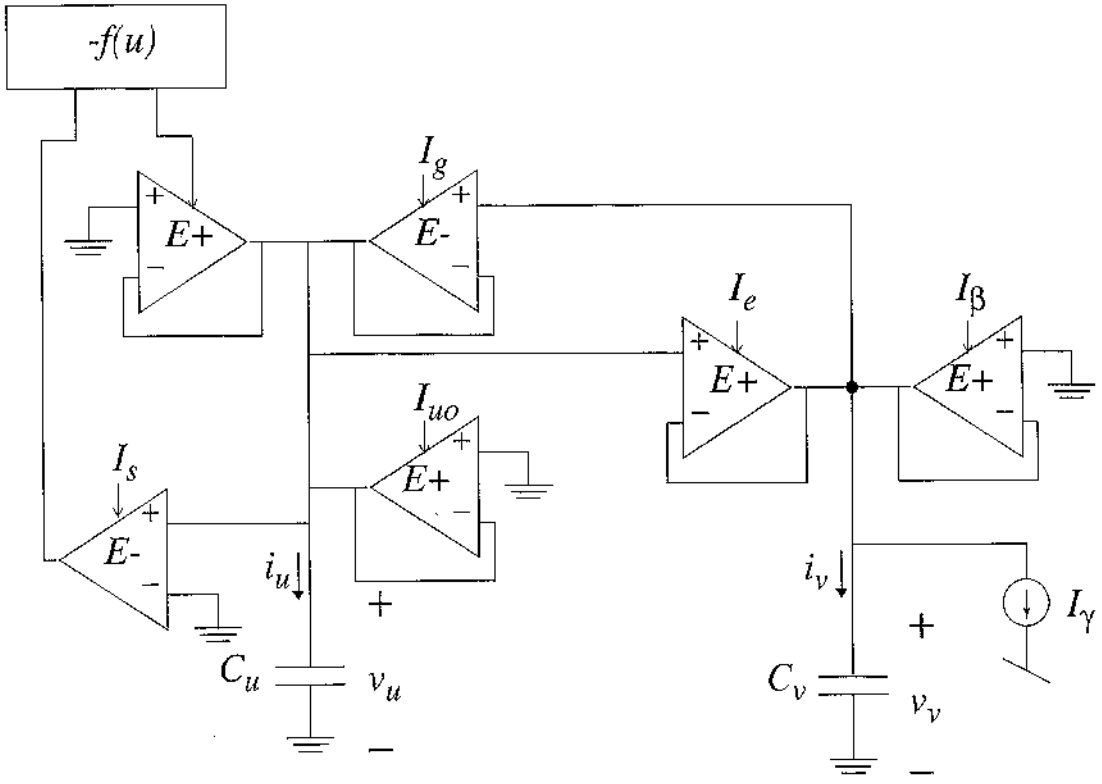


*Figure 7.* Block diagram of the second order circuit implementing Eq. (14).

transconductors depends exponentially on the difference between the positive and negative controlling voltages. Figure 8(a) shows the schematic of the bipolar implementation of the positive $E$-element. The circuit in Fig. 8(a) belongs to the class of translinear networks [25]. Using a reformulation of the translinear principle [26], this circuit can be easily analyzed. It is found that the circuit in Fig. 8(a) gives an output current,

$$I_o = I_b \exp\left(\frac{v_+ - v_-}{2v_t}\right), \tag{15}$$

where $v_t$ is the thermal voltage.

Figure 8(b) shows the implementation of an $E$-element using MOS transistors operating in the subthreshold regime. The circuit in Fig. 8(b) verifies also an exact translinear relationship giving an output current,

$$I_o = I_b \exp\left(\frac{\kappa_p(v_+ - v_-)}{2v_t}\right), \tag{16}$$

where $\kappa_p$ is a PMOS subthreshold parameter [24].

The negative $E$-element, $E-$, is equivalent to the positive one but giving a negative output current. That is, the current flowing out of the negative $E$-element is,

$$I_o = -I_b \exp\left(\frac{\kappa_p(v_+ - v_-)}{2v_t}\right). \tag{17}$$

The negative $E$-element can be implemented using the same circuits used for the positive one (see Fig. 8) but taking current $I_o^-$ as the output current instead of current $I_o^+$.[1]

It is easy to show that with this selection of the transconductance elements, the circuit of Fig. 7 implements the system of differential equations given by (14) with

$$\alpha = \frac{\kappa_p}{2v_t}. \tag{18}$$

The block denoted as $-f(u)$ in Fig. 7 implements in current mode the piecewise-linear nonlinearity shown in Fig. 1. A negative $E$-element biased by a current $I_s$ and controlled by the voltage difference $v_+ - v_- = v_u$ (see Fig. 7) provides a sinking current $u = I_s \exp(\alpha v_u)$. This current is used as the input of the nonlinear block $-f(u)$. Figure 9 depicts the schematic of a current mode circuit implementing such nonlinear block. The output current $-f(u)$ of this nonlinear block is the

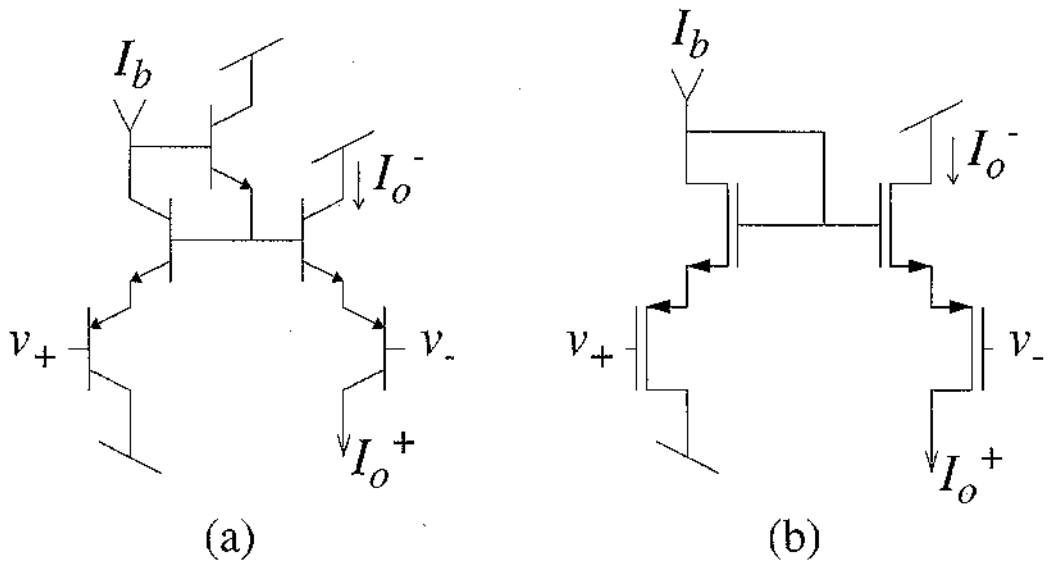


*Figure 8.* Positive E element $E+$, (a) bipolar implementation, and (b) subthreshold MOS implementation.

bias current of a positive $E$-element controlled by a voltage difference $v_+ - v_- = -v_u$. Hence, a current term $(-f(u))\exp(-\alpha v_u)$ is fed into the $C_u$ capacitor as required in Eq. (14).

### *V.B. Coupling Between Cells*

To implement the coupling terms among cells in Eq. (12) eight additional $E$-elements are required per cell: four $E$-elements to couple the $v_u(i, j)$ voltage of cell $(i, j)$ with the $v_u$ voltages of its four nearest neighbors $v_u(i-1, j)$, $v_u(i+1, j)$, $v_u(i, j-1)$, $v_u(i, j+1)$; and four other $E$-elements to couple the $v_v(i, j)$ voltage of each cell $(i, j)$ with the $v_v$ voltage of its four nearest neighbors $v_v(i-1, j)$, $v_v(i+1, j)$, $v_v(i, j-1)$, $v_v(i, j+1)$. Figure 10 shows a diagram of the extra blocks needed to implement the coupling terms that appear in Eq. (12).

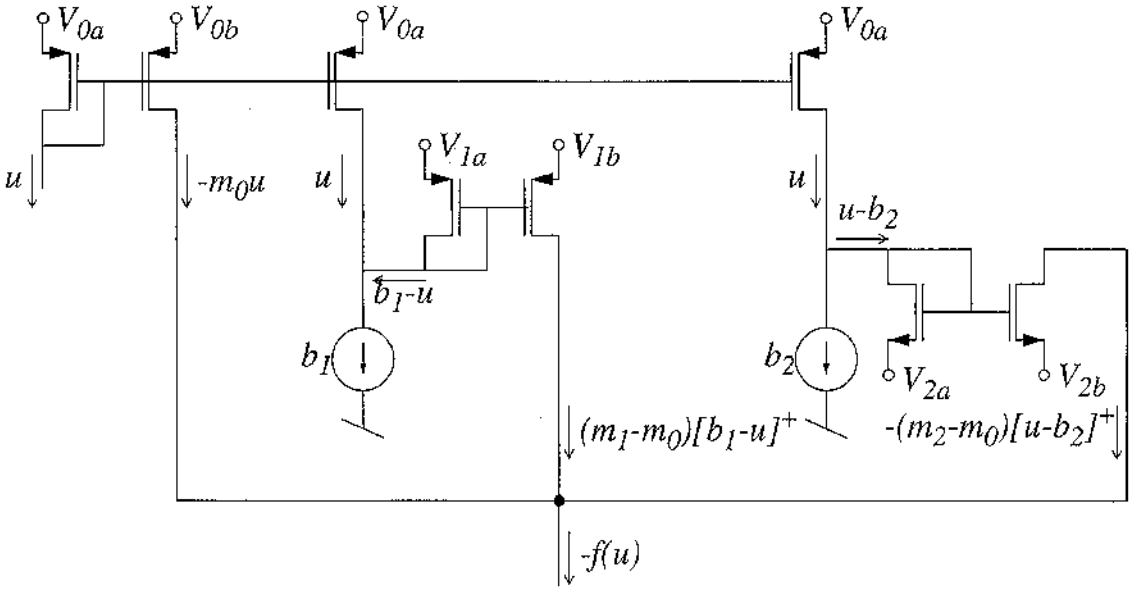


*Figure 9.* Current mode implementation of the piecewise-linear nonlinearity.

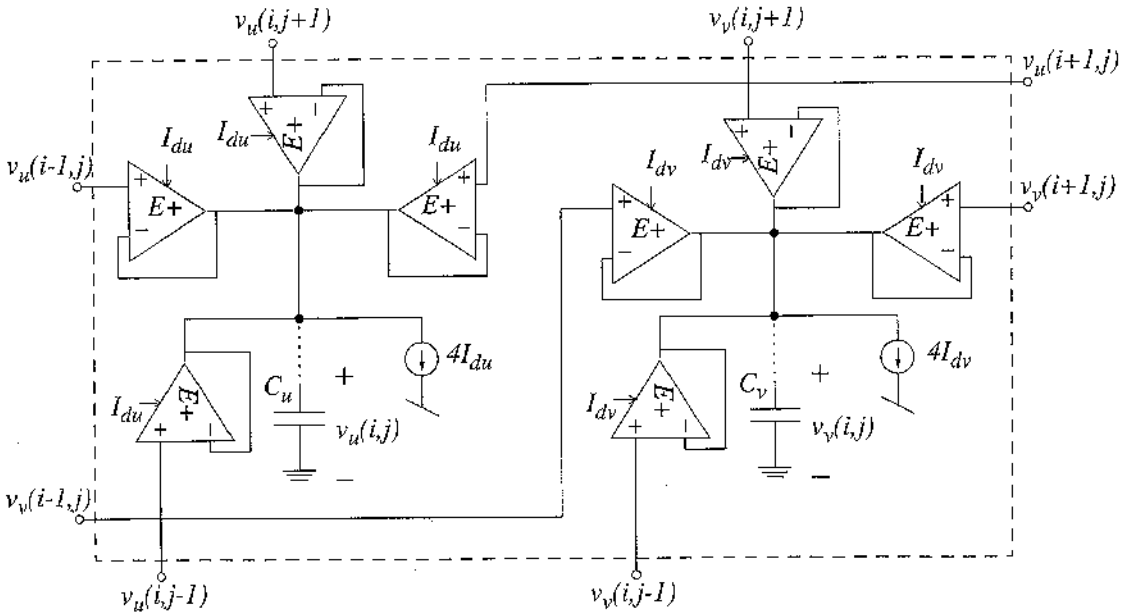


*Figure 10.* Extra blocks needed to implement the coupling terms between cells.

### V.C. *Initial Conditions Circuitry*

To generate the different spatio-temporal behaviors simulated in Section III, appropriate initial conditions must be set in the $u$ and $v$ state variables of all the cells in the array. In all the simulations of Section III, binary initial conditions were used. That is, each cell in the array is set to either one of two possible initial states $(u_{0_1}, v_{0_1})$ or $(u_{0_2}, v_{0_2})$.

In our design, we sequentially set the initial values of the $u$ and $v$ state variables to one of two possible continuously programmable states $(u_{0_1}, v_{0_1})$ or $(u_{0_2}, v_{0_2})$. Afterwards, the system switches to its normal evolution mode and the different spatio-temporal behaviors illustrated in Section III are generated on chip. A careful design of the initial conditions circuitry is needed in order to avoid erasing or modification of the stored initial states during this switching. This switching problem is particularly severe in log-domain operation where the $u$ and $v$ state variables depend exponentially on the log-compressed $v_u$ and $v_v$ voltages stored on capacitors $C_u$ and $C_v$. Small deviations of $v_{u_0}$ or $v_{v_0}$ due to charge injection during the switching are exponentially amplified producing large errors in the initial state. Hence, avoiding any feedthrough injection during switching is essential for correct operation.

Figure 11(a) depicts a block diagram of the circuitry added to set the initial conditions in the $v_u$ and $v_v$ voltages. A set of inverters configured as a shift register selects which initial conditions $(u_{0_1}, v_{0_1})$ or $(u_{0_2}, v_{0_2})$ are set in each cell. Figure 11(b) shows the schematic of the boxed block in Fig. 11(a) that sets the initial voltage $v_{0_i}$ (or $u_{0_i}$) in cell capacitor $C_u$ (or $C_v$). In Fig. 11(b), $v_{sb}$ and $v_{sc}$ are two switched voltages. $v_{sc}$ switches from $v_{dd}$, when the initiation signal $ic$ is high, to $V_{dd} - 1V$, when signal $ic$ is low (normal operation mode). Signal $v_{sb}$ switches from $V_{ss}$, when $ic$ is high, to $V_{ss} + 1V$, when $ic$ is low. When signal $ic$ is high the initial conditions are being set in the cells. During this period, all the components in the circuit are disconnected from nodes $v_u$ (or $v_v$), except one of the boxed elements of Fig. 11(a). In the steady state, when the input current to capacitor $C_u$ (or $C_v$) is zero, the output current of the negative $E$-element (current $i_{oe}$ is Fig. 11(b)), is forced to be equal to the supplied current $u_{0_i}$ (or $v_{0_i}$). Hence the output voltage $v_o$ (which is connected to capacitor nodes $v_u$ or $v_v$) is forced to be,

$$v_u = \frac{1}{\alpha} \ln\left(\frac{u_{0_i}}{I_s}\right), \tag{19}$$

and hence,

$$u_{0_i} = I_s \exp(\alpha v_u). \tag{20}$$

When signal $ic$ is low, currents $u_{0_i}$ (or $v_{0_i}$) and $i_{oe}$ are cut off. The switching of the currents is done by switching

the source terminals of the current supplying transistors, with their gate terminal being kept at constant voltages. This switching strategy avoids any undesired charge injection in the output node [27].

As explained before, during the setting of the initial conditions all the other components in the circuit must be delivering a zero output current to the $v_u$ and $v_v$ nodes. This can be achieved by substituting all the $E$-elements and current sources in Figs. 7 and 10 by switched $E$-elements and switched current sources. The schematic of a switched positive $E$-element is shown in Fig. 12(a). Figure 12(b) shows the schematic of the switched negative $E$-element. And Fig. 12(c) depicts the schematic of a switched sinking current source. Note that all the switching is done through the sources of the output current supplying transistors

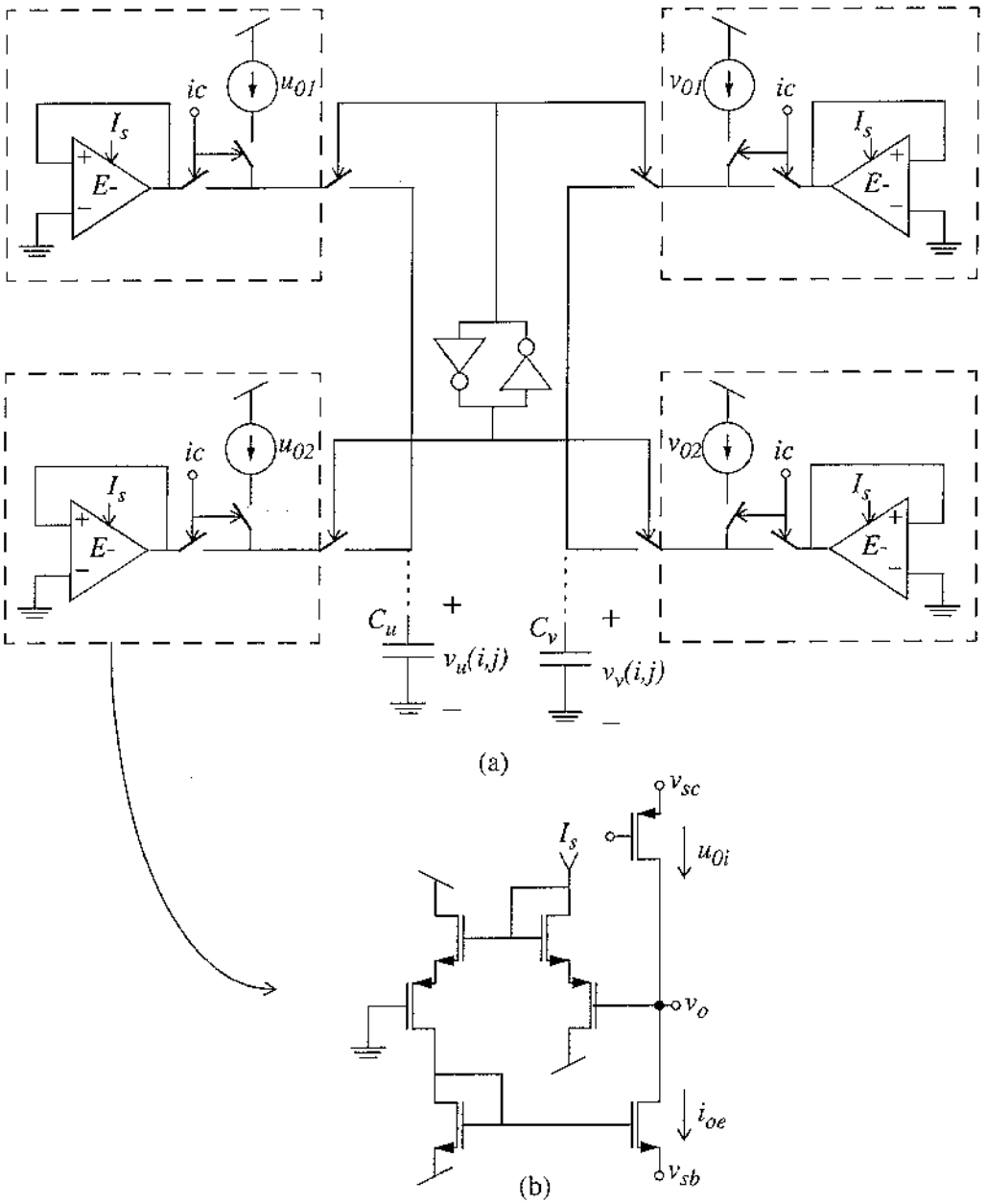


*Figure 11.* (a) Block diagram of the initial conditions circuitry, and (b) schematic of the boxed block in Fig. 11(a).

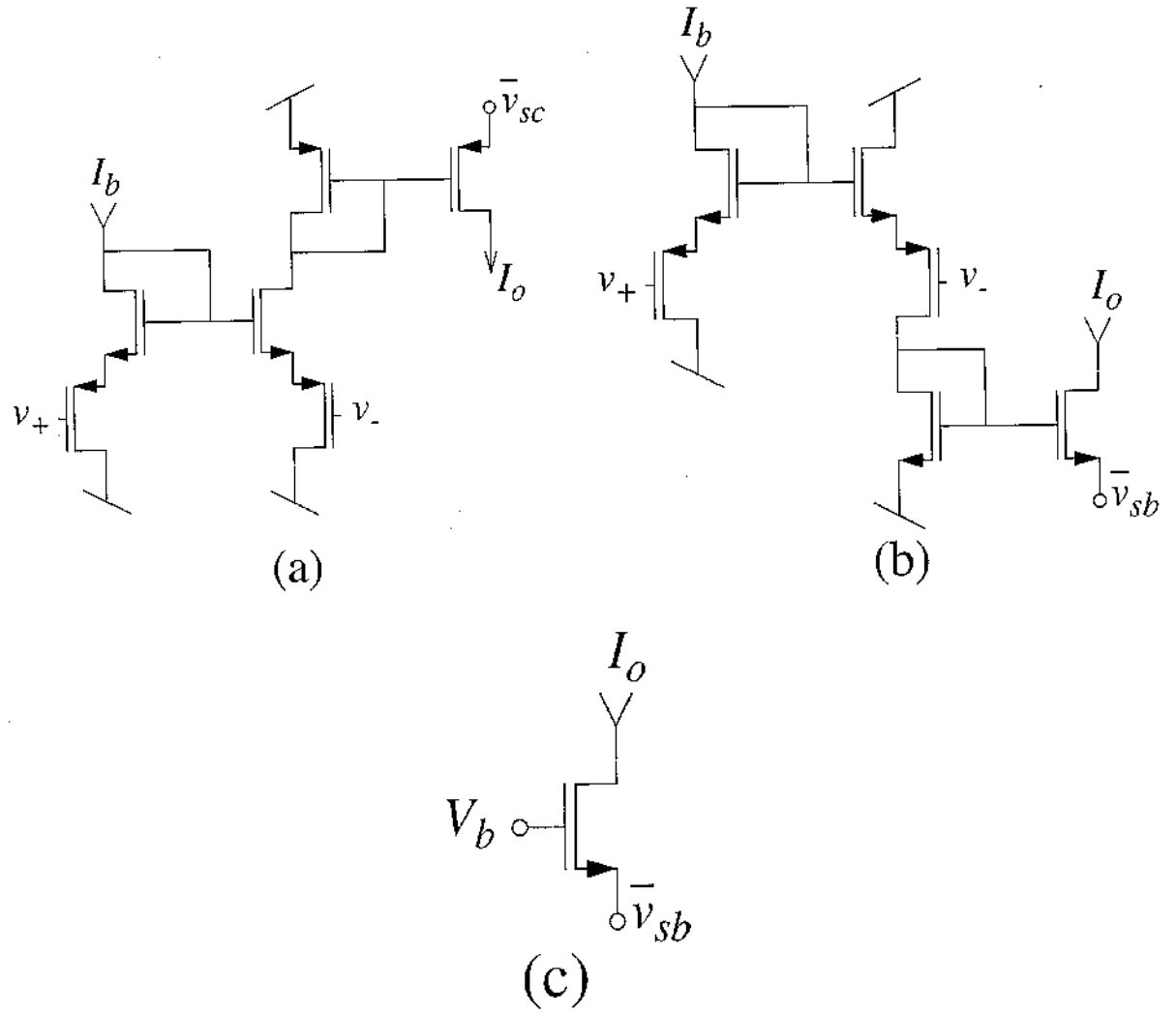


*Figure 12.* Schematics of (a) switched $E+$ -element, (b) switched $E-$ -element, and (c) switched current source.

to avoid any charge injection in the capacitors during switching [27].

## VI. Simulation Results

In this section we present results of HSPICE simulations of the circuit described in Section V. Simulations of an uncoupled cell and of a one dimensional array of 32 coupled cells have been performed. All HSPICE simulation results have been compared with the results of MATLAB simulations of the ideal reaction diffusion CNN obeying the discretely spaced version of Eq. (8). A very good agreement between the results of both simulations has been found in all the cases. Thus, validating the correct operation of the hardware described in Section V.

### *VI.A. The Uncoupled Cell*

The correct operation of the cells described in subsection V.A. has been verified. To do that, we have compared the null isoclines of an uncoupled cell obeying differential equation (8) with the null isoclines of the circuit of Fig. 7 obtained through HSPICE simulations.

To obtain the null isoclines of the circuit shown in Fig. 7 through HSPICE simulations, the following procedure has been followed:

1. Capacitors $C_u$ and $C_v$ of Fig. 7 are substituted by ideal voltage sources $v_u$ and $v_v$.
2. A DC analysis of the resulting circuit is done in HSPICE. In the simulation, a two dimensional sweep of voltages $v_u$ and $v_v$ is done. In the

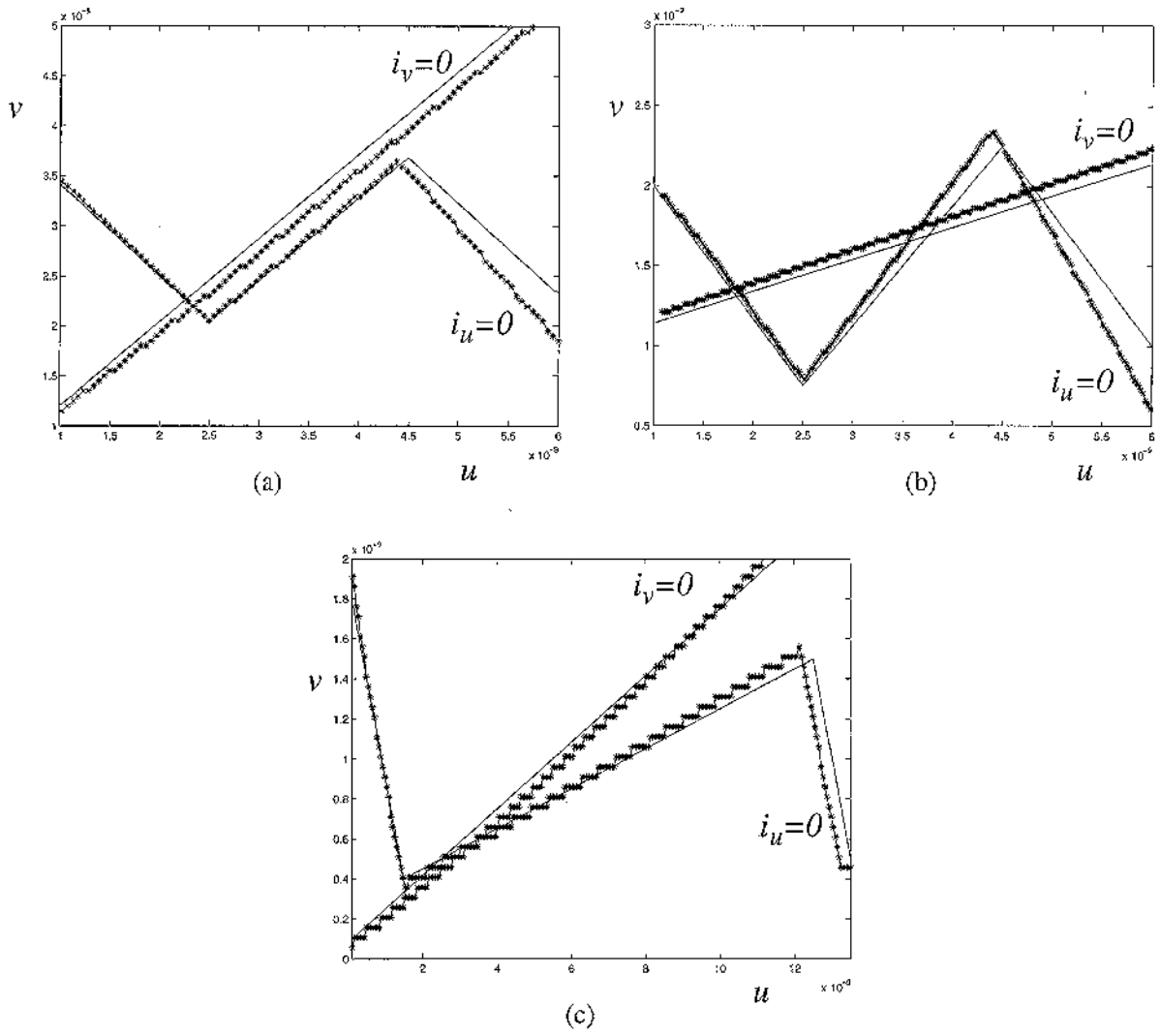


*Figure 13.* Comparison between the null isoclines obtained through MATLAB and through HSPICE simulations for different settings of the cell parameters.

analysis, the total currents flowing into nodes $v_u$ and $v_v$ ($i_u$ and $i_v$ in Fig. 7) are taken as outputs.

3. For each value of $v_u$ (or equivalently of the $u = I_s \exp(\alpha v_u)$ state variable), we look for the corresponding values of $v_v$ (or equivalently of the $v = I_s \exp(\alpha v_v)$ state variable) such that currents $i_u$ and $i_v$ become zero. These two values of $v$ correspond, respectively, to the points that belong to the isocline curves $\dot{u} = 0$ and $\dot{v} = 0$, for that given value of $u$.

Figure 13 shows the null isoclines obtained through HSPICE simulations for different settings of the circuit parameters. Also shown in Fig. 13 are the null isoclines of the uncoupled cell that obeys differential Eq. (8).

In the simulation of Fig. 13(a) the cell parameters are set to emulate an excitable medium [28]. That is, each cell has a unique equilibrium point. Under perturbation, the cells become excited and go back to their stable equilibrium point after a refractory period. The continuous traces in Fig. 13(a) are the null isoclines curves derived from Eq. (8) for the cell parameters: $m_1 = 1$, $m_2 = 1$, $m_0 = -0.9$, $b_1 = 25 \times 10^{-9}$, $b_2 = 45 \times 10^{-9}$, $\beta n = 4.5 \times 10^{-9}$, $\gamma = 1.2$, $g = 1.1$, $v_{\text{off}} = 0$ and $u_{\text{off}} = 0$. The traces marked with asterix correspond to the null isoclines obtained through HSPICE simulations for circuit parameters: $I_s = 1$ nA, $I_e = 1$ nA, $I_\beta = 4.5$ nA,

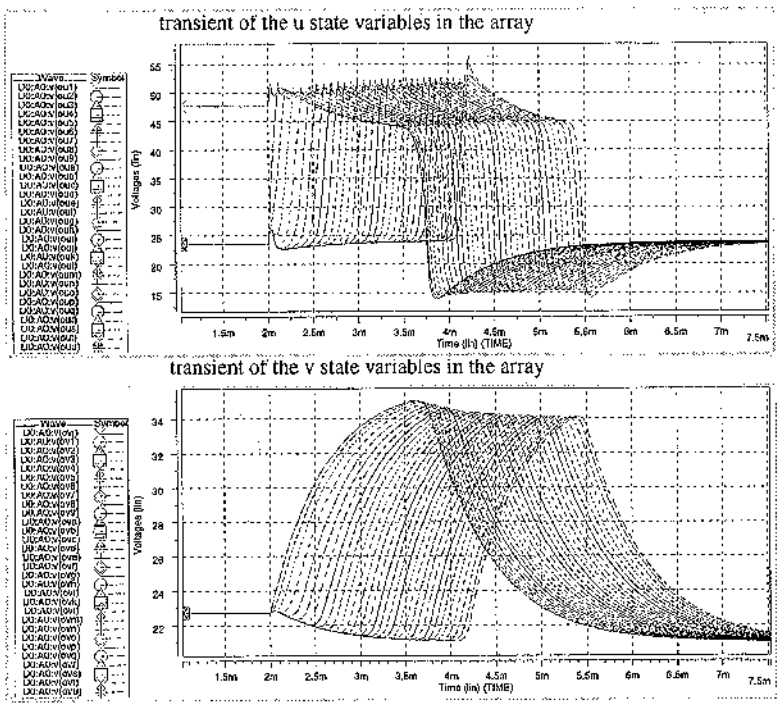


(a)

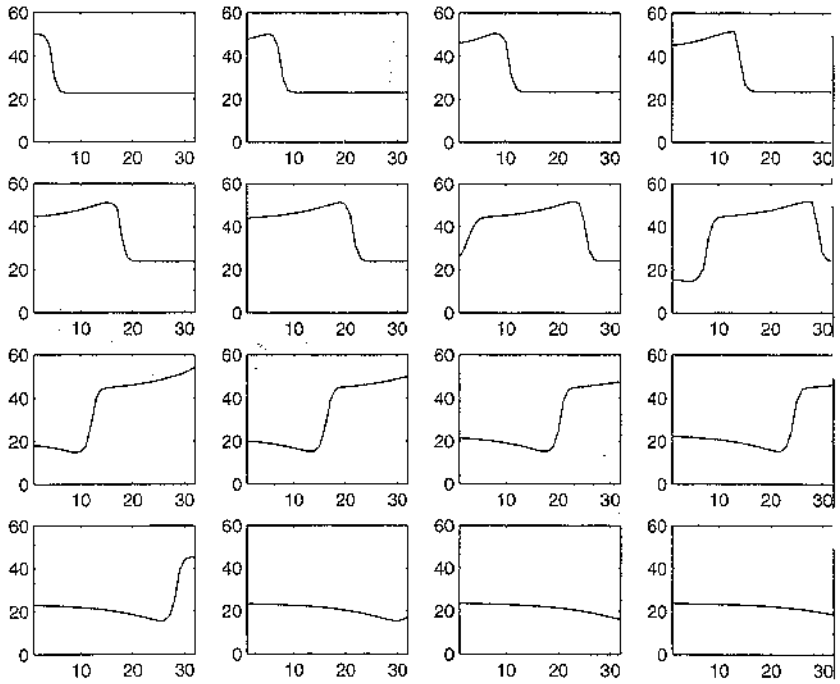

(b)

*Figure 14.* HSPICE simulation of a traveling wave propagating in a one dimensional array of 32 cells. (a) Waveforms of the $u$ and $v$ state variables versus time, and (b) snapshots of the $u$ state variables observed every 250 $\mu$s. (c) MATLAB simulations of the same propagating wave. Snapshots of the $u$ state variable observed every 250 $\mu$s

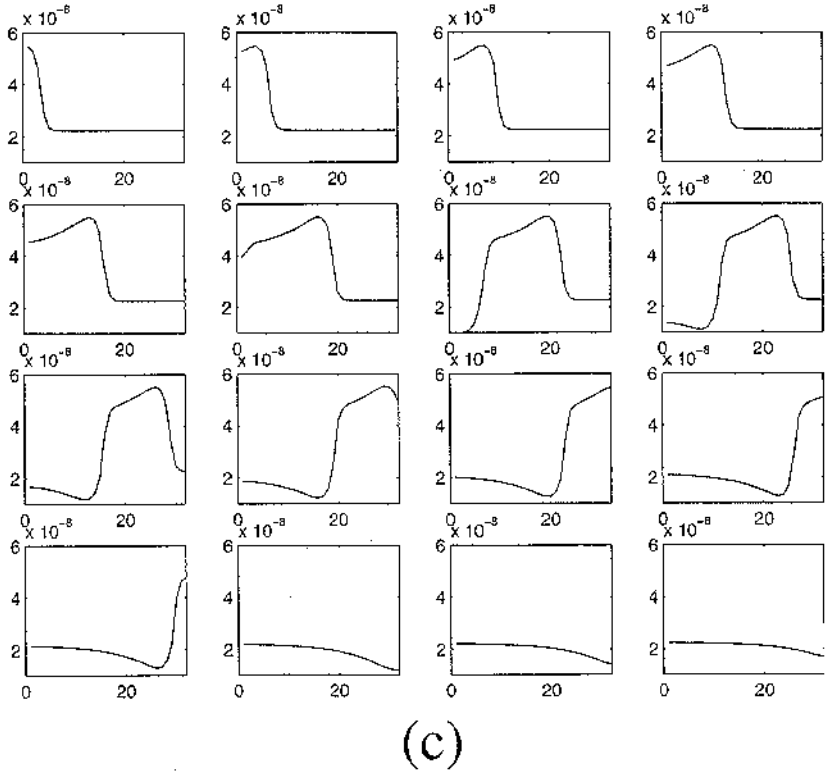


*Figure 14.* Continued.

$I_\gamma = 1.2\,\text{nA}$, $I_g = 1.1\,\text{nA}$, $I_{uo} = 0$, and for the nonlinear block parameters, $m_1 = 1$, $m_2 = 1$, $m_0 = -0.9$, $b_1 = 25\,\text{nA}$, $b_2 = 45\,\text{nA}$. The circuit parameters are related with the original cell parameters through Eq. (13). Figure 13(a) shows a very good agreement between the null isoclines and the equilibrium point of the differential Eq. (8) and the equation implemented with the log-domain circuit simulated with HSPICE.

In the simulation of Fig. 13(b) the cell parameters are set to emulate a biestable medium [28]. That is, each uncoupled cell has two stable equilibrium points. Under perturbation the cells can trigger from one equilibrium point to the other. The continuous traces in Fig. 13(b) are the null isoclines curves derived from Eq. (8) for cell parameters: $m_1 = 1$, $m_2 = 1$, $m_0 = -0.9$, $b_1 = 2.5 \times 10^{-9}$, $b_2 = 4.5 \times 10^{-9}$, $\beta n = 0.7 \times 10^{-9}$, $\gamma = 5$, $g = 1.2$, $v_{\text{off}} = 4 \times 10^{-9}$ and $u_{\text{off}} = -1.35 \times 10^{-9}$. The traces marked with asterix correspond to the null isoclines obtained through HSPICE simulations for circuit parameters: $I_s = 1\,\text{nA}$, $I_e = 1\,\text{nA}$, $I_\beta = 4.7\,\text{nA}$, $I_\gamma = 5\,\text{nA}$, $I_g = 1.2\,\text{nA}$, $I_{uo} = -1.35\,\text{nA}$,[2] and for the nonlinear block parameters, $m_1 = 1$, $m_2 = 1$, $m_0 = -0.9$, $b_1 = 2.5\,\text{nA}$, $b_2 = 4.5\,\text{nA}$. It can be verified that the circuit parameters are again related with the original cell parameters through Eq. (13).

For the simulation of Fig. 13(c) the cell parameters are set such that the cells have a unique equilibrium point which is stable for one uncoupled cell, but becomes unstable under certain coupling conditions [17]. The continuous traces in Fig. 13(b) are the null isoclines curves derived from Eq. (8) for the cell parameters: $m_1 = 1$, $m_2 = 1$, $m_0 = -0.1$, $b_1 = 1.5 \times 10^{-9}$, $b_2 = 12.5 \times 10^{-9}$, $\beta n = 0$, $\gamma = 6$, $g = 1$, $v_{\text{off}} = 0.5 \times 10^{-9}$ and $u_{\text{off}} = 0.25 \times 10^{-9}$. The traces marked with asterix correspond to the null isoclines obtained through HSPICE simulations for circuit parameters: $I_s = 1\,\text{nA}$, $I_e = 1\,\text{nA}$, $I_\beta = 0.5\,\text{nA}$, $I_\gamma = 6\,\text{nA}$, $I_g = 1\,\text{nA}$, $I_{uo} = 0.25\,\text{nA}$, and for the nonlinear block parameters, $m_1 = 1$, $m_2 = 1$, $m_0 = -0.1$, $b_1 = 1.5\,\text{nA}$, $b_2 = 12.5\,\text{nA}$.

### *VI.B. One Dimensional Array of Cells*

We have performed HSPICE simulations of a one dimensional array of 32 coupled cells. Each cell is coupled to its two nearest neighbors with the coupling strategy shown in Fig. 10.

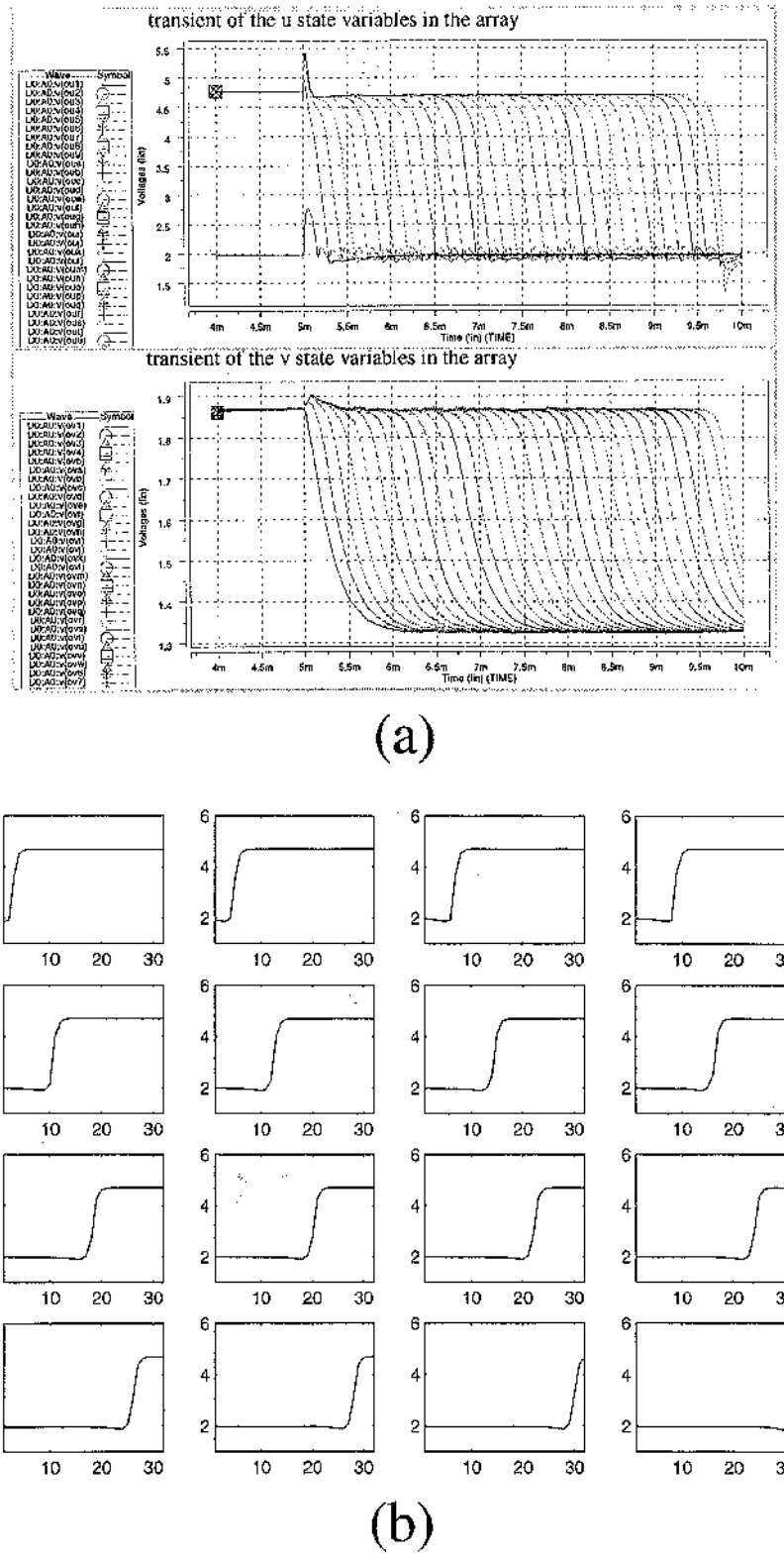


*Figure 15.* HSPICE simulation of a trigger wave propagating in a one dimensional array of 32 cells. (a) Waveforms of the $u$ and $v$ state variables versus time, and (b) snapshots of the $u$ state variable observed every 250 $\mu$s. (c) MATLAB simulations of the same propagating wave. Snapshots of the $u$ state variable observed every 250 $\mu$s.

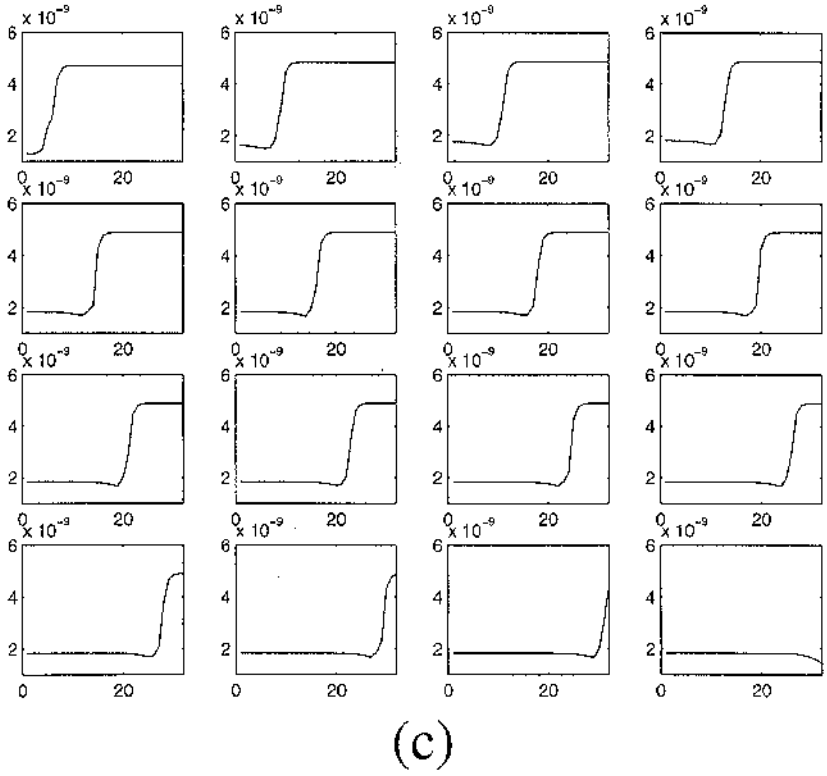


*Figure 15.* Continued.

In this Section we show simulation results for two different settings of cell parameters that reproduce two different spatio-temporal behaviors: a traveling wave and a trigger wave propagation.

Figure 14(c) shows results from a MATLAB simulation of a traveling wave propagating in a one dimensional array of 32 cells. In this simulation, a linear array of coupled cells obeying the spatially discretized version of Eq. (8) was considered. The cell parameters were set to $\tau = 42\,\mu s$, $\varepsilon = 1/35$, $m_1 = 1$, $m_2 = 1$, $m_0 = -0.9$, $b_1 = 25 \times 10^{-9}$, $b_2 = 45 \times 10^{-9}$, $\beta n = 4.5 \times 10^{-9}$, $\gamma = 1.2$, $g = 1.1$, $v_{\text{off}} = 0$ and $u_{\text{off}} = 0$. The coupling parameters were $D_u = 0.5$ and $D_v = 0$. Figure 14(c) shows the snapshots of the $u$ state variable observed every 250 $\mu s$.

Figure 14(a) and (b) show results of an HSPICE simulation of the travelling wave behavior. The circuit parameters in the simulation of Fig. 14(a) and (b) are the following: $C_u = 0.5$ pF, $C_v = 17.5$ pF, $I_s = 1$ nA, $I_e = 1$ nA, $I_\beta = 4.5$ nA, $I_\gamma = 1.2$ nA, $I_g = 1.1$ nA, $I_{uo} = 0$, for the nonlinear block, $m_1 = 1$, $m_2 = 1$, $m_0 = -0.9$, $b_1 = 25$ nA, $b_2 = 45$ nA, and for the coupling elements $I_{du} = 0.5$ nA, and $I_{dv} = 0$. This circuit implements the spatially discretized version of differential Eq. (8). The equivalent cell parameters are the same used in the simulation of Fig. 14(c). Figure 14(a) shows the waveforms obtained with HSPICE of the $u$ and $v$ state variable of the 32 cells in the array. Figure 14(b) shows snapshots of the $u$ state variable observed every 250 $\mu s$.

Figure 15(c) shows results of a MATLAB simulation of a trigger wave propagating in a one dimensional array of 32 cells. A linear array of coupled cells obeying the spatially discretized version of Eq. (8) was simulated. The cell parameters were set to $\tau = 42\,\mu s$, $\varepsilon = 1/35$, $m_1 = 1$, $m_2 = 1$, $m_0 = -0.9$, $b_1 = 2.5 \times 10^{-9}$, $b_2 = 4.5 \times 10^{-9}$, $\beta n = 4.7 \times 10^{-9}$, $\gamma = 5$, $g = 1.2$, $v_{\text{off}} = 0$ and $u_{\text{off}} = -1.35 \times 10^{-9}$. The coupling parameters were $D_u = 0.5$ and $D_v = 0$. Figure 15(c) shows the snapshots of the $u$ state variable observed every 250 $\mu s$.

Figure 15(a) and (b) show results of an HSPICE simulation of a trigger wave. The circuit parameters in the simulation of Fig. 15(a) and (b) are the following: $C_u = 0.5$ pF, $C_v = 17.5$ pF, $I_s = 1$ nA, $I_e = 1$ nA, $I_\beta = 4.7$ nA, $I_\gamma = 5$ nA, $I_g = 1.2$ nA, $I_{uo} = -1.35$ nA, for the nonlinear block, $m_1 = 1$, $m_2 = 1$, $m_0 = -0.9$, $b_1 = 2.5$ nA, $b_2 = 4.5$ nA, and for the coupling

elements $I_{du} = 0.5$ nA, and $I_{dv} = 0$. This circuit implements the spatially discretized version of differential Eq. (8). The equivalent cell parameters are the same used in the simulation of Fig. 15(c). Figure 15(a) shows the waveforms obtained with HSPICE of the $u$ and $v$ state variable of the 32 cells in the array. Figure 15(b) shows snapshots of the $u$ state variable observed every 250 $\mu$s.

## VII. Conclusions

A second order reaction-diffusion equation has been selected which has been shown to be the simplest equation able to generate, through parameter setting, trigger wave, traveling wave propagation, spiral wave and Turing pattern formation.

A set of parameters has been identified that reproduce each of these behaviors when the selected equation is spatially discretized and implemented with an array of $N \times N = 32 \times 32$ cells of second order dynamics.

It has been verified that all the behaviors are robust against random variations of the cell parameters with a standard deviation higher than $\sigma = 20\%$. This robustness in the behavior makes it suitable to be reproduced by a specialized hardware.

A hardware implementing the spatially discretized version of the selected equation has been designed. In the hardware implementation the cell state variables are logarithmically encoded as voltages stored in some capacitors. This logarithmic compression of the state variables allows several decades of variation of these state variables without saturation of the elements and with low distortion. All the parameters of the implemented equation are set as biasing currents that can be adjusted several decades. Furthermore, by scaling some biasing currents of the circuit the time constant of the implemented equation can also be appropriately scaled. This can be helpful to make the waveforms generated on chip easily observable and for some applications where an extremely slow time constant may be needed (i.e. in locomotion applications).

The correct operation of the designed hardware has been verified through HSPICE simulations. HSPICE simulations of a traveling wave and a trigger wave propagating in a one dimensional array of 32 cells have been performed. The results of these simulations have been compared with MATLAB simulations of the corresponding differential equation. An extremely good agreement between both behaviors has been observed.

## Acknowledgments

This work was partially supported by ONR research grant "Design of High Density and Neuromorphic CNN Universal Chips as Image Microprocessors."

## Notes

1. Frey proposes to implement the negative $E$-element by substituting each transistor in Fig. 8(a) by its complementary, thus inverting the sign of every current in the circuit of Fig. 8(a) [21]. However, this solution is not valid for the MOS implementation. In the MOS case, if we substitute the PMOS pair of the circuit of Fig. 8(b) by its complementary in the negative $E$-elements, we obtain different $\alpha$ parameters (see Eq. (18)) for the positive and negative terms of Eq. (14). However, one can note that in the circuits of Fig. 8 an output current of opposite sign $I_o^-$ is also available from a high impedance node of the output branch.
2. To implement the negative $I_{uo}$, the $E+$-element in Fig. 7 must be replaced by a $E-$-element biased by $|I_{uo}|$.

## References

1. L.O. Chua, M. Hasler, G.S. Moschytz, and J. Neirynck, "Autonomous cellular neural networks: A unified paradigm for pattern formation and active wave propagation," *IEEE Transactions on Circuits and Systems, Part I*, Vol. 42, No. 10, pp. 559–577, Oct. 1995.
2. V.I. Krinsky, V.N. Biktashev, and I.R. Efimov, "Autowaves principles for parallel image processing," *Physica D*, Vol. 49, pp. 247–253, 1991.
3. M. de Castro, M. Gómez-Gesteira, and V. Pérez-Villar, "Influence of the distance on the interaction between an autonomous pacemaker and a reentry," *Physical Review E*, Vol. 57, No. 1, pp. 949–953, Jan. 1998.
4. I. Pérez-Mariño, M.de Castro, V. Pérez-Muñuzuri, M. Gómez-Gesteira, L.O. Chua, and V. Pérez-Villar, "Study of reentry initiation in coupled parallel fibers," *IEEE Transactions on Circuits and Systems, Part I*, Vol. 42, No. 10, pp. 665–671, Oct. 1995.
5. V.N. Biktashev and A.V. Holden, "Re-entrant waves and their elimination in a model of mammalian ventricular tissue," *Chaos*, Vol. 8, No. 1, pp. 48–56, 1998.
6. V.N. Biktashev, A.V. Holden, and H. Zhang, "A model for the action of external current onto excitable tissue," *International Journal of Bifurcation and Chaos*, Vol. 7, No. 2, pp. 477–485, 1997.
7. V.S. Zykov, *Simulation of Wave Processes in Excitable Media*, Manchester University Press, Manchester, 1987.
8. J.D. Murray, *Mathematical Biology*, Springer-Verlag, New York, 1989.
9. R.A. Fisher, "The wave of advance of advantageous genes," *Ann. Eugenics*, Vol. 7, pp. 355–369, 1937.

10. R. FitzHugh, "Mathematical models of excitation and propagation nerve," *in Biological Engineering*, H. Schwan (Ed.) McGraw-Hill, New York, 1969.
11. A.L. Hodgkin and A.F. Huxley, "A quantitative description of membrane current and its application to conduction and excitation in nerve," *Journal of Physiology*, Vol. 117, pp. 500–544, 1952.
12. J.J. Thyson, "The Belousov-Zhabotinskii Reaction," *Lecture Notes in Biomathematics*, Vol. 10, Springer-Verlag, New York, 1976.
13. A.M. Turing, "The chemical basis of morphogenesis," *Philos. Trans. R. Soc. London, Ser. B*, Vol. 237, pp. 37–72, 1952.
14. R.J. Field and R.M. Noyes, "Oscillations in chemical systems, IV. Limit cycle behavior in a model of a real chemical reaction," *J. Chem. Phys.*, Vol. 60, pp. 1877–1884, March 1974.
15. A. Pérez-Muñuzuri, V. Pérez-Muñuzuri, V. Pérez-Villar, and L.O. Chua, "Spiral waves on a 2-D array of nonlinear circuits," *IEEE Transactions on Circuits and Systems, Part I*, Vol. 40, No. 11, Nov. 1993.
16. V. Pérez-Muñuzuri, V. Pérez-Villar, and L.O. Chua, "Autowaves for image processing on a two-dimensional CNN array of excitable nonlinear circuits: flat and wrinkled labyrinths," *IEEE Transactions on Circuits and Systems, Part I*, Vol. 40, No. 3, March 1993.
17. L. Goras, L.O. Chua, and D.M.W. Leenaerts, "Turing patterns in CNNs-Part I: Once over lighty," *IEEE Transactions on Circuits and Systems, Part I*, Vol. 42, No. 10, pp. 612–626, Oct. 1995.
18. M. Delgado-Restituto, A. Rodríguez-Vázquez and F. Vidal, "Nonlinear synthesis using ICs," in *Encyclopedia of Electrical and Electronic Engineering*, J. Webster (Ed.), John Wiley and Sons, 1999.
19. D.R. Frey, "State-space synthesis and analysis of log-domain filters," *IEEE Transactions on Circuits and Systems, Part II*, Vol. 45, No. 9, 1205–1211, Sept. 1998.
20. D.R. Frey, "Log-domain filtering: An approach to current mode filtering," *Proceedings of the Institute of the Electrical Engineers*, Vol. 140, Pt. G, No. 6, pp. 406–416, Dec. 1996.
21. D.R. Frey, "Exponential state space filters: A generic current mode design strategy," *IEEE Transactions on Circuits and Systems, Part I*, Vol. 43, pp. 34–42, Jan. 1996.
22. Special section on instantaneous companding in analog signal processing, *IEEE Transactions on Circuits and Systems, Part II*, Vol. 45, No. 9, Sept. 1998.
23. E. Vittoz and J. Fellrath, "CMOS analog integrated circuits based on weak inversion operation," *IEEE Journal of Solid State Circuits*, Vol. SC-12, pp. 224–231, June 1997.
24. A.G. Andreou and K.A. Boahen, "Translinear circuits in subthreshold MOS," *Analog Integrated Circuits and Signal Processing*, Vol. 9, pp. 141–166, 1996.
25. B. Gilbert, "Translinear circuits: A proposed classification," *Electronics Letters*, Vol. 11, No. 1, pp. 14–16, 1975; errata, Vol. 11, No. 6, p. 136.
26. B.L. Hart, "Translinear circuit principle: A reformulation," *Electronics Letters*, Vol. 15, No. 24, pp. 801–803, Nov. 1979.
27. G. Cauwenberghs and A. Yariv, "Fault-tolerant dynamic multilevel storage in analog VLSI," *IEEE Transactions on Circuits and Systems, Part II*, Vol. 41, No. 12, pp. 827–829, 1994.
28. L. Pivka, "Autowaves and spatio-temporal chaos in CNNs-PART I: a tutorial," *IEEE Transactions on Circuits and Systems, Part I*, Vol. 42, No. 10, Oct. 1995.

**Teresa Serrano-Gotarredona** received the B.S. degree in electronic physics in June 1992 from the University of Seville, Sevilla, Spain. She received the Ph.D. degree in VLSI neural categorizers from the University of Seville in December 1996, after completing all her research at the Analog Design Department of the National Microelectronics Center (CNM), Sevilla, Spain. From September 1996 until August 1997, she obtained an M.S. degree in the Department of Electrical and Computer Engineering of the Johns Hopkins University, Baltimore, MD, where she was sponsored by a Fulbright Fellowship. Presently she is a research staff member of the Analog Design Department of the National Microelectronics Center in Sevilla, Spain. Her research interests include analog circuit design of linear and nonlinear circuits, VLSI neural based pattern recognition systems, VLSI implementations of neural computing and sensory systems, and VLSI electrical parameter characterization. Dr. Serrano-Gotarredona was corecipient of the 1995–96 IEEE Transactions on VLSI Systems Best Paper Award for the paper "A Real-Time Clustering Microchip Neural Engine". He is co-author of the book "Adaptive Resonance Theory Microchips".
email: terese@imse.cnm.es

**Angel Rodríguez-Vázquez**, *IEEE Fellow*, is a Professor of Electronics at the Department of Electronics and Electromagnetism (University of Seville). He is also a member of the research staff of the Institute of Microelectronics of Seville—Centro Nacional de Microelectrónica (IMSE-CNM)—where he is heading a research group on Analog and Mixed-Signal VLSI. His research interests are in the design of analog interfaces for mixed-signal VLSI circuits, CMOS imagers and vision chips, neuro-fuzzy controllers, symbolic analysis of analog integrated circuits and optimization of analog integrated circuits. Dr. Rodríguez-Vázquez served as an Associate Editor of the IEEE Transactions on Circuits and Systems-I form 1993 to 1995, as Guest Editor of the IEEE TCAS-I special issue on "Low-Voltage and Low-Power Analog and Mixed-Signal Circuits and Systems" (1995), as Guest Editor of the IEEE TCAS-II special issue on "Advances in Nonlinear Electronic Circuits" (1999), and as chair of the IEEE-CAS Analog Signal Processing Committee (1996). He was co-recipient of the 1995 Guillemin-Cauer award of the IEEE Circuit and Systems Society, and the best paper award of the 1995 European Conference on Circuit Theory and Design. In 1992 he received also the young scientist award of the Seville Academy of Science. In 1996 he was elected to the degree of Fellow of the IEEE for "contributions to the design and applications of analog/digital nonlinear ICs".
email: angel@imse.cnm.es